XFEM Simulation of Radial-Median Crack Evolution in Knoop Indentation of Brittle Materials

Felix Rickhey*, Jin Haeng Lee**, and Hyungyil Lee*

* Dept. of Mechanical Engineering, Sogang University, Seoul, S. Korea
** Division for Research Reactor, Korea Atomic Energy Research Institute, Daejeon, S. Korea

Abstract: In sharp indentation of brittle materials, a complex three-dimensional stress field evolves in the material beneath the indenter and may cause cracking. During unloading, a tensile residual stress field drives the crack to its final semi-elliptical shape. The so-induced crack can be used for e.g. crack growth experiments, but for which the initial crack size and shape have to be known. For the analysis of the crack evolution in a material subject to a complex stress field, which changes with position, time and crack advancement, the extended finite element method (XFEM) represents a useful tool. We analyze the formation of the crack occurring during Knoop indentation of brittle materials. Issues associated with XFEM in Abaqus/Standard are discussed for the problem at hand, and suggestions are made with regard to meshing, the artificially attributed viscosity parameter, and the damage-initiating stress threshold. Finally we discuss the influence of material properties on the fracture toughness evaluation. Results can be used for predicting fracture toughness and final crack shape.

Keywords: Knoop Indentation; Brittle Materials; Fracture Toughness; XFEM

1. Introduction

The indentation test has become a popular method for determining the fracture toughness of brittle materials. Its main advantage over other standard methods is that it can be more or less directly applied to structures with a flat surface; specimen preparation is thereby reduced to a minimum, and pre-cracks are not required.

In Knoop indentation of brittle materials, a median crack is initiated during loading (high loads) or during unloading (lower load range). While the crack grows due to the increasing applied load during loading, during unloading it is driven by a growing residual stress field caused by the increasing mismatch between the plastic zone and the outer elastic zone, which is trying to reduce in size. For fracture mechanics analyses, the Knoop indentation crack has usually been treated as a 2D elliptical crack subject to a point load at the center of the indentation (Keer 1986). The probably most cited work on Knoop indentation cracking was conducted by Marshall (1983). His analysis was based on the well-known equation by Lawn, Marshall and Evans (Lawn 1980), which relates mode I fracture toughness K_c to maximum indentation load $P_{\max}$ and surface crack length c (Figure 1) measured from the loading axis in outward radial direction

$$K_c = \chi \frac{P_{\max}}{c^{3/2}} \, . \tag{1}$$

The constant χ can be understood as the relative strength of the residual field that drives the crack and was reported to be a function of the ratio of Young's modulus E to hardness H. Subsequent studies yet revealed that Equation (1) may be inaccurate owing to an oversimplification of the stress field (*e.g.* Ponton 1989a,b; Quin 2007; Lee 2012; Hyun 2014).

Knoop indentation differs from Vickers or Berkovich indentation insofar as (1) only one crack forms (hence no interaction of radial-median cracks); (2) the plastic zone has approximately the shape of a prolate spheroid, whose major axis is nearly as long as the major impression diagonal $2a$. Based on experiments with Si_3N_4, Marshall (1983) found that the point-load assumption inherent in Equation (1) holds also for Knoop indentation, provided a sufficiently high load. The threshold for Equation (1) to be applicable was defined by a crack length-to-impression half-diagonal ratio $c/a \geq \sim 1.3$ (which however applies only to the tested material). Knoop indentation cracks are much larger than Vickers indentation cracks at equal $P_{\max}$, as Petrovic (1983) concluded in a similar study from Knoop indentation tests on glass-ceramic (C9606). Keer (1986) attempted at a 3D fracture analysis taking into account the large aspect ratio of the Knoop indenter and the resulting elongated plastic zone. Lube (2001) conducted Vickers and Knoop indentation tests on a gas pressure sintered silicon nitride and analyzed the shape of resulting cracks and how it is influenced by $P_{\max}$.

The single sharp and rather short crack can be advantageous because it is more amenable to the analyses of fracture, surface flaws or residual stresses (Ahn 1996). Further, crack growth experiments can be conducted on Knoop crack-induced specimens to determine the material's R-curve after removal of a thin surface layer containing the core zone. However, in order to use Knoop indentation cracks as starter cracks, we need to be able to predict the size and shape of the induced crack as a function of material properties. In this study, we first present an XFEM-based model that allows the simulation of Knoop indentation cracking and discuss critical issues associated with cohesive zone-based XFEM. We then study the crack evolution for a Si-like reference material and discuss the influence of friction and material properties on parameter χ. The results are to serve to better understand the crack evolution, and to explain phenomena occurring in Knoop indentation cracking tests.

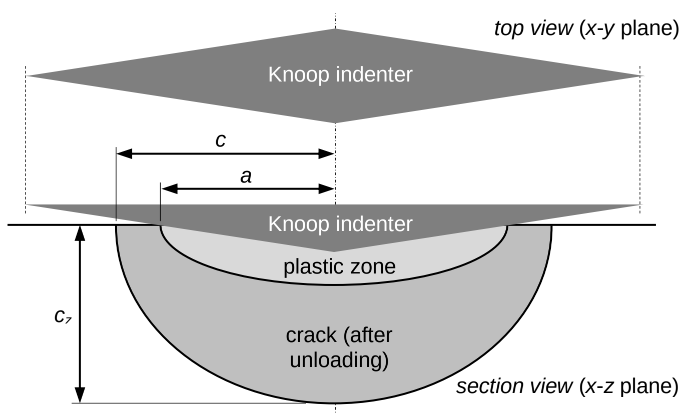

Figure 1. Semi-elliptical configuration of plastic zone and Knoop indentation crack.

2. XFE model

The XFE model for Knoop indentation cracking is shown in Figure 2. Considering geometric and loading symmetries, modeling one half of the specimen is sufficient. Symmetry constraints with respect to the two indenter diagonal planes are imposed. The bottom nodes are fixed. The model features a relatively fine mesh in the inner region, where all damage is expected to occur, and an outer region, the mesh of which gradually coarsens in outward radial direction. As diamond or WC indenters, whose Young's moduli are much higher than that of the material to be indented, are usually employed in indentation cracking tests, for simplicity and to keep computational costs low the indenter is assumed rigid. In the contact between indenter and material, the node-to-surface contact pair option (Abaqus 2013) gives a more realistic and accurate contact distribution and is therefore preferred. Coulomb friction is considered by $\mu = 0.2$, which is representative of the contact of diamond with various types of materials. The whole FE model consists of $\approx 2\times10^5$ 8-node brick elements (C3D8).

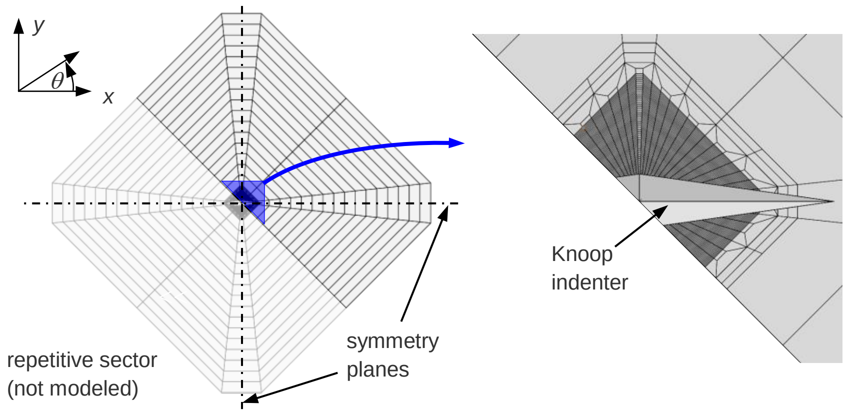

Figure 2. Half model for Knoop indentation cracking.

2.1 Mesh

In XFEM, it is generally problematic when a crack propagates along an element edge because this may lead to instability (Mohammadi 2008). As major damage is supposed to occur in the planes normal to the surface and through the indenter diagonals – indenter edges act as stress raisers –, the mesh is structured so that no nodes are placed in the indenter diagonal planes. In connection with XFEM, Abaqus allows the use of 8 node brick elements only. Although two nodes can be placed at one position, damage cannot be initiated between these two nodes. A slender cylindrical segment (with the cylinder axis aligned with the z-axis) of radius $r_c = 0.02e$ is therefore removed from the center of the model. The innermost nodes, *i.e.* nodes with radial distance r_c from the loading axis, are constrained in circumferential (θ) direction. FE results (enrichment deactivated) obtained using two models – one with $r_c = 0$, one with $r_c = 0.02e$ –yield a negligible difference in the load-depth curves, and maximum principal stresses are observed in the same element at the same depth. Further, variation of r_c in the range $r_c/e = [0.005, 0.05]$ does not affect crack shape and size.

Using only one enriched zone (EZ) for the inner region we observed that damage propagation ceases during the analysis and that damage does not initiate in other regions although stresses are well beyond the damage initiating threshold. However, by dividing the inner region into several EZ, which are arranged such that elements of one and the same EZ do not share nodes (Figure 3), we observe smooth damage propagation and even merging. Eight EZ are necessary here, four for a median element section (EZ 1-4) and four for the neighboring median section (EZ 5-8), and then again EZ 1-4 (not displayed in Figure 3).

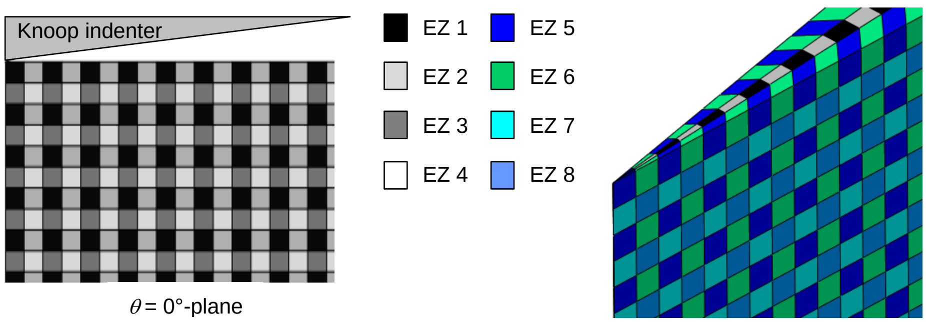

Figure 3. Arrangement of enriched zones (EZ) in the inner region.

2.2 Material model

The material is assumed to be isotropic and exhibit elastic-perfectly plastic behavior. Indeed, the compressive behavior of many brittle materials can be accurately described by the elastic-perfectly plastic material model (Francois 1988). Yielding occurs according to the associated flow rule using the Mises potential, and plastic deformation is volume-conserving. Mode I fracture toughness K_c remains constant (flat R curve), as is the case for an ideally brittle material (Anderson 2004). A reference material is defined with E = 200 GPa, ν = 0.3 and σ_y = 5.0 GPa and fracture energy Γ = 3.0 MPa μm, values that are close to Si and that were also used by Lee (2012). Since all materials used in this study have a high hardness-to-Young's modulus ratio (H/E), fracture is assumed to occur in the framework of linear elastic fracture mechanics (LEFM).

Damage initiation is governed by the maximum normal stress (σ) criterion which states that damage initiates when the condition

$$\langle \sigma \rangle = \hat{\sigma} \tag{2}$$

is met at the centroid of an element; the resulting damage plane is oriented normal to σ (Abaqus, 2013). $\hat{\sigma}$ is the damage-initiating stress threshold and $\langle \ldots \rangle$ denotes the Macaulay brackets. To prevent potential lateral cracking, which is often observed in indentation, only stresses normal to median planes are considered damage-causing. It is to be noted that damage initiation is mesh-dependent, and the exact time of initiation cannot be determined accurately. However, the eventual goal here is to find the final crack shape, which is hardly influenced by the time of initiation.

Damage propagation occurs according to a traction-separation law, which governs the stiffness degradation – represented by damage variable D – associated with an incremental increase in crack opening displacement (Figure 4). Hutchinson (2000) showed that the shape of the curve is of secondary importance, so that we use the simplest, bilinear, form. The fracture energy is equal to the area below the traction-separation curve

$$\Gamma = \frac{1}{2}\hat{\sigma}\,\delta_c\,, \tag{3}$$

where δ_c is the critical displacement, beyond which the stiffness is degraded to zero. The damage zone is defined by the region where $\hat{\delta} < \delta < \delta_c$. $\hat{\delta}$ is the displacement corresponding to $\hat{\sigma}$. Assuming plane strain conditions and linear softening, its length L_{DZ} is (Rice 1968; Tomar 2004)

$$L_{DZ} \approx \frac{\pi}{8}\frac{\Gamma E'}{\hat{\sigma}^2}\,, \tag{4}$$

where $E' = E/(1-\nu^2)$ for plane strain, and ν is Poisson's ratio. Fracture energy Γ is related to K_c by $\Gamma = K_c / E'$. Since material softening may lead to severe convergence problems, a small viscosity ζ is introduced to the material model (Gao 2004). The meaning and significance of the parameters $\hat{\sigma}$, ζ and L_{DZ} will be discussed below.

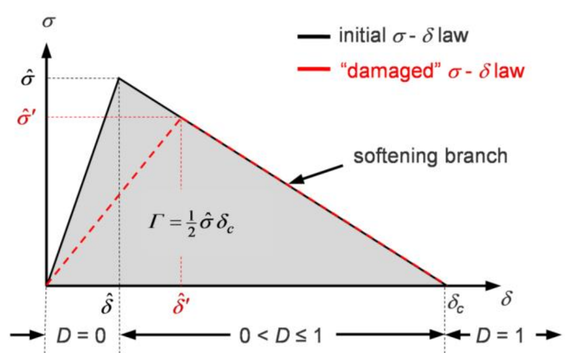

Figure 4. Traction-separation (σ- δ) law constituting damage.

3. FE results for Knoop indentation cracking

3.1 General aspects of Knoop indentation crack evolution

Indentation is performed on the reference material ($\Gamma = 3.0$ MPa μm, $\hat{\sigma} = 0.8$ GPa) applying P_{max} = 480 mN. Cracking occurs exclusively in the long diagonal plane ($\theta = 0°$); only a small damage at the surface (but no crack) is observed in the $\theta = 90°$ median plane (Figure 5). The crack initiates on the *z*-axis as a subsurface crack, grows in outward radial direction during the loading cycle without penetrating the surface. Shortly after load reversal, the crack penetrates the surface.

Varying h_{max} = [0.4, 1.0] μm (Γ = 3.0 MPa μm) and Γ = [1.5, 7.0] MPa μm (h_{max} = 0.8 μm), we find that for $h_{max} \leq 0.4$ μm, the crack does not open up to the surface; it seems that in order for the crack to open up its length inside the material at load reversal must be > ~ a (or the length of the plastic zone). For $h_{max} \geq 0.8$ μm or $\Gamma \leq 4.0$ MPa μm, $P_{max}/c^{3/2}$ is constant above a threshold of $c/a \approx 1.2$ (Figure 6). This supports the experimental observation that the point-load assumption can be used provided a sufficiently high P_{max}. Marshall (1983) found from experiments with Si_3N_4 that Equation (1) is valid for $c/a \geq \sim 1.3$ (but where a was measured after unloading). However, experiments reveal that in general the c/a threshold increases with E/H and K_c. If c/a is below the threshold, application of Equation (1) results in an underestimation of K_c. In contrast to Vickers indentation, once a surface crack occurs, we can be sure that the crack is of half-penny shape.

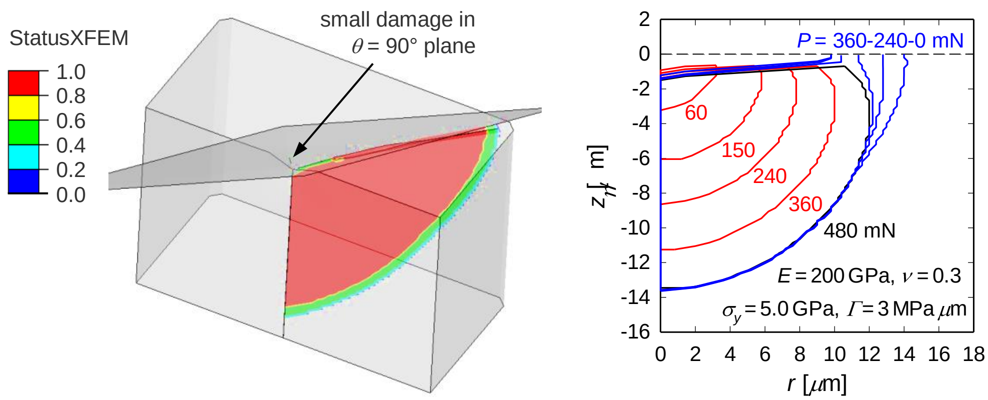

Figure 5. Crack evolution applying Pmax = 480 mN: loading cycle (red), unloading cycle (blue) (left); final crack in Abaqus/Viewer (right).

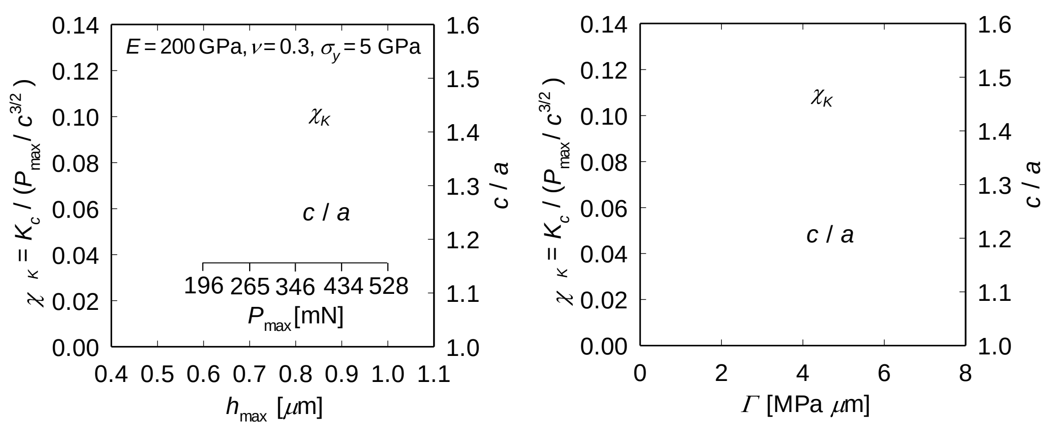

Figure 6. Change of χ_K with maximum indentation depth h_{max} and fracture energy Γ.

Having obtained $H_K = P_{max}/A_c = 11.2$ GPa (A_c is contact area at P_{max}) from a separate FE analysis with a refined mesh ($h_{max}/e = 12.5$ μm) and making use of the relation $\chi_K = \alpha_K (E/H_K)^{1/2}$, where α_K is a proportionality factor (subscript K denotes the reference to Knoop indentation), α_K

approaches a constant value of 0.0251, which is higher than the value obtained by Marshall (1983), α_K = 0.0229. However our reference material differs in material properties such as ν, which α_K (or χ_K) is sensitive to, as will be shown later.

3.2 Load-displacement curve

FE results follow Kick's law ($P \propto h^2$, h is indentation depth; Fischer-Cripps 2002) very accurately (Figure 7). Cracking makes $P_{\max}$ decrease only slightly– 2 % for the reference material –, which can be explained by the very low damage energy E_{dmg} relative to the energy dissipated by plastic deformation, E_{PD} ($E_{dmg} \approx 0.01\ E_{PD}$).

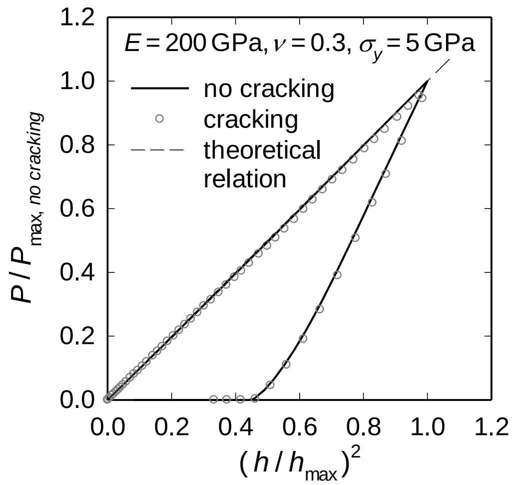

Figure 7. Load-depth data confirm the theoretical relation $P \propto h^2$; cracking hardly affects the load-depth curve ($h_{\max}$ = 1.0 μm).

3.3 Relation between damage-initiating stress threshold $\hat{\sigma}$ and damage zone length LDZ

The (bi-) linear cohesive zone law of a material is constituted by two independent material parameters: fracture energy Γ and the damage-initiating stress threshold $\hat{\sigma}$, which indicates the brittleness of the material, *e.g.* for an ideally brittle material $\hat{\sigma} \rightarrow \infty$ (no damage zone). On the one hand L_{DZ} must be large enough to reach convergence, and on the other hand small enough to comply with LEFM. Considering computational costs, L_{DZ} / e should be small. A small e may further result in an extreme stress peak at first contact and premature damage, which does not occur in real indentation due to tip rounding. Further, convergence necessitates L_{DZ} to be minimum 2e (Moës 2002). We find that with L_{DZ}/e values between 1 and 2, convergence can be reached, but at the expense of a significant increase in computational costs, while even lower L_{DZ}/e lead to an underestimation of c. Consequently, a trade-off must be made between a sufficiently high $\hat{\sigma}$ and a reasonable mesh density in the inner region. Since a lower $\hat{\sigma}$ gives a lower crack length but a larger damage zone, the crack length for an ideally brittle material, c^*, must be $c < c^* < c + L_{DZ}$ (where c is the crack length corresponding to a finite $\hat{\sigma}$). c^* can thus be approached by lowering e

and at the same time increasing $\hat{\sigma}$ while keeping in mind that $L_{DZ} \geq 2e$. Note also that a too high $\hat{\sigma}$ inhibits damage initiation since maximum tensile stresses are limited by $1/3\sigma_y$.

Assuming $\hat{\sigma}$ = 0.5, 0.8, 1.1 and 1.2 GPa, XFE analysis results using the reference material are summarized in Table 1. The crack and damage shapes as well as E_{dmg} are hardly influenced by $\hat{\sigma}$ (Figure 8). The damage zone size obtained by FE results is in agreement with the theoretical value obtained by Equation (4). As expected from above discussion, the crack length c increases with $\hat{\sigma}$ and approaches, while L_{DZ} decreases; for $\hat{\sigma}$ = 1.2 GPa the damage zone is only 1.5 % of the crack length; yet $L_{DZ} < 2e$. A method for estimating c^* is given in the Appendix.

In this study we choose $\hat{\sigma}$ = 0.8 GPa, which gives on the one hand a small damage zone and on the other hand good convergence and relatively low computational costs. However the brittleness $\hat{\sigma}$ is a material property and exerts some influence on χ_K.

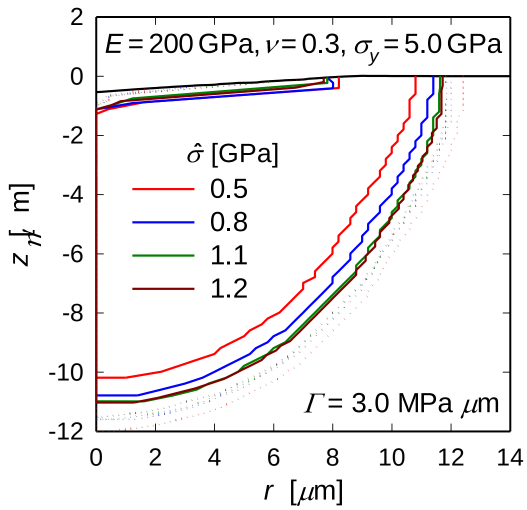

Figure 8. Damage (dotted lines) and crack (solid lines) shapes for diverse $\hat{\sigma}$ at load reversal (semi-transparent) and after full unloading.

Table 1. Damage parameters for diverse $\hat{\sigma}$ (E = 200 GPa, ν = 0.3, σ_y = 5.0 GPa, Γ = 3.0 MPa μm, h_{max} = 0.8 μm).

$\hat{\sigma}$ [GPa]	P_{max} [mN]	c [μm]	L_{DZ} [μm]	L_{DZ} (FE) [μm]	L_{DZ} / e	L_{DZ} / c	χ_K
0.5	339.3	10.84	1.04	1.1	5.2	0.096	0.0854
0.8	345.0	11.44	0.40	0.5	2.0	0.035	0.0911
1.1	345.2	11.62	0.21	0.2	1.1	0.018	0.0932
1.2	346.2	11.72	0.17	0.1	1.0	0.015	0.0936

3.4 Viscous regularization

Models exhibiting softening behavior are susceptible to severe convergence difficulties because the element stiffness tensor may cease to be positive definite. Gao and Bower (2004) showed that the problem can be mitigated by viscous regularization damping. For the reference material the range of appropriate viscosity values ζ that yield identical crack sizes and shapes is investigated (Table 2). Plotting the energy dissipated by damage, E_{dmg} (normalized by E_{dmg} for $\zeta = 10^{-6}$ after unloading), over indenter position $h/h_{\max}$, we find that even for relatively high values ($\zeta = 1 \times 10^{-4}$), accurate crack shapes are obtained (Figure 9). Higher ζ values however retard crack evolution and give highly inaccurate crack areas. On the other hand, analysis time generally decreases with increasing ζ; in this particular case it drops between 10^{-5} and 10^{-4}. In this study we use $\zeta = 5 \times 10^{-5}$ to provide accuracy and at the same time relatively fast convergence. However, it is expedient to check if E_{dmg} still rises shortly after detachment of the indenter from specimen.

Table 2. Damage parameters for diverse ζ (E = 200 GPa, ν = 0.35, σ_y = 5.0 GPa, Γ = 3.0 MPa μm, $\hat{\sigma}$ = 0.8 GPa, $h_{\max}$ = 0.7 μm).

ζ	c [μm]	c_z [μm]	E_{dmg} [nJ]	$E^{tot}_{dmg} / E^{tot}_{dmg,\zeta=10^{-6}}$	χ_K
1e–6	9.64	8.91	0.391	1.00	0.0909
1e–5	9.64	8.91	0.391	1.00	0.0909
1e–4	9.63	8.86	0.390	0.99	0.0904
5e–4	9.50	7.92	0.351	0.90	0.0870

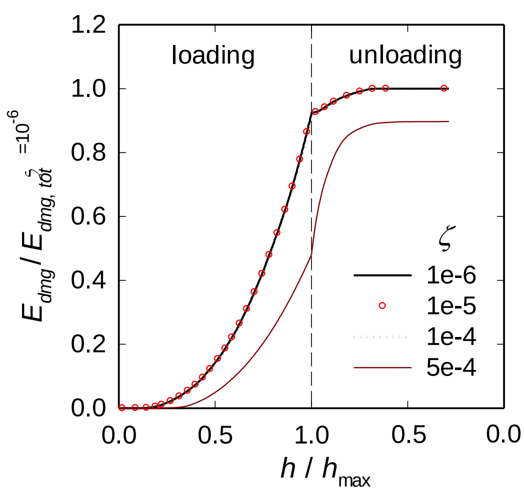

Figure 9. Influence of viscosity value ζ on energy dissipated by damage, E_{dmg}.

3.5 Influence of friction between indenter and material

Lawn (1975) interpreted the influence of friction in indentation theory as an increase of the indenter angle φ by a friction-dependent term $\pm$ arctan μ (+ for loading; – for unloading), which means that friction has a crack driving force-decreasing effect during loading (lower wedging forces) and a driving force-raising effect during unloading (higher wedging forces). XFE results for μ = [0, 0.4] (h_{max} = 0.8 μm) confirm this trend partly (Figure 10). While during loading frictionless contact does not lead to a larger crack, during unloading the increased wedging forces due to friction make the final crack slightly larger than the one resulting from frictionless contact. The friction effect on c is to some part balanced by a decrease in P_{max}, so that the sensitivity of χ_K to μ is rather low (Table 3). The crack shape is not affected by friction.

Further, the influence of friction has an upper limit. No further increase in the final crack size can be observed when raising μ from 0.2 to 0.4, which is because for $\mu \geq 0.2$ the contact type of a surface node changes from slipping to sticking immediately after first contact. E_{dmg} and c do not increase either. The frictional effect on c is however too small to be considered quantitatively.

Table 3. Influence of friction (E = 200 GPa, ν = 0.3, Γ = 3.0 MPa µm, h_{max} = 0.8 µm).

μ	c [µm]	P_{max} [mN]	E_{dmg} [nJ]	χ_K
0.0	10.6	336.1	0.508	0.0840
0.1	10.9	338.6	0.534	0.0860
0.2	11.0	339.4	0.536	0.0870
0.4	11.0	339.4	0.536	0.0871

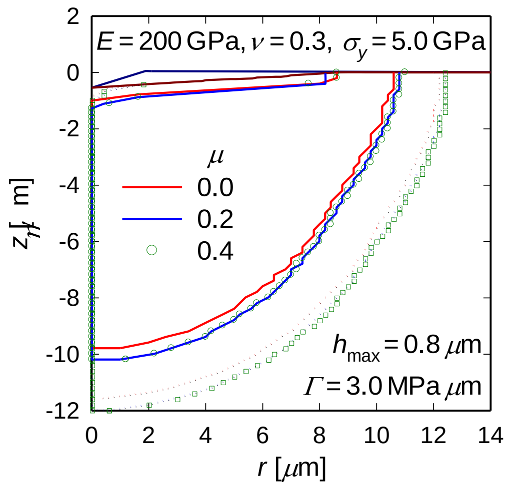

Figure 10. Damage (semi-transparent) and crack shapes at load reversal (dotted/squares) and after full unloading (solid lines/circles).

4. Influence of Poisson's ratio, Young's modulus and yield strain

Based on analytical considerations, Lawn (1980) arrived at $\chi \propto (E/H)^{1/2} \cot^{2/3}\varphi$; the derivation however bases on an oversimplified stress field and the neglect of Poisson's ratio, which affect the plastic zone shape and the crack driving forces. For Vickers and Berkovich indentation, the problem was investigated by Lee (2012) and Hyun (2014). In this final section, we investigate the sensitivity of χ_K to E, ν and σ_y. The results can be used to establish functions that map material properties to χ_K.

Parameter studies are performed for combinations of E = {100, 200, 300, 400, 600} GPa; ν = {0.0, 0.1, 0.2, 0.3, 0.35}; σ_y = {3, 5, 8} GPa. The change of χ_K with E and ν is plotted in Figure 11 for the three σ_y values. For the silicon nitride used by Marshall (1983) (E = 300 GPa, ν = 0.24, σ_y = 7.8 GPa[1]), we get by interpolation $\chi_K \approx 0.089$, which is close to the experimental value of 0.096.

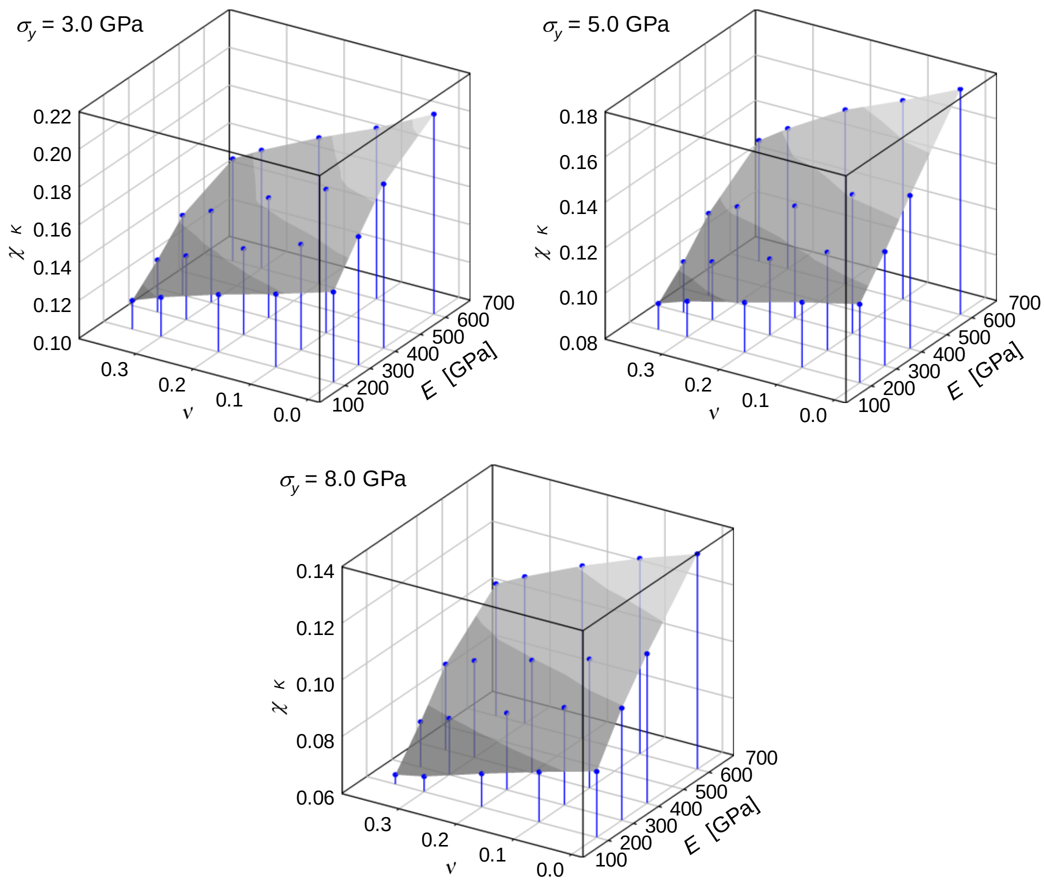

Figure 11. Change of coefficient χ_K with E and ν for σ_y = 3.0, 5.0 and 8.0 GPa.

[1] σ_y is found by varying its value until the resulting hardness matches the given Vickers hardness of H = 18.5 GPa.

Generally, the crack lengths c_A and c_B from indentations applying equal P_{max} on two materials (A and B) with equal Γ are related by

$$P_{max}\big|_A = P_{max}\big|_B \quad \leftrightarrow \quad \frac{c_A}{c_B} = \left(\frac{\chi_{KA}}{\chi_{KB}}\right)^{2/3} \left(\frac{E_B}{E_A}\frac{1-\nu_A^2}{1-\nu_B^2}\right)^{1/3} \tag{5}$$

Based on FE results (Figure 11) and Equation (5), the following trends for Knoop indentation cracking can be deduced. Comparing two materials that vary only in their

(1) ν values: $\nu_A > \nu_B$, $\chi_{KA} < \chi_{KB} \rightarrow c_A < c_B$ (smaller $\nu \rightarrow$ larger crack)
(2) σ_y values: $\sigma_{yA} > \sigma_{yB}$ ($H_{KA} > H_{KB}$), $\chi_{KA} < \chi_{KB} \rightarrow c_A < c_B$ (smaller $\sigma_y \rightarrow$ larger crack)
(3) E values: $E_A > E_B$, $\chi_{KA} > \chi_{KB}$, $c_A < c_B$

Whereas (1) and (2) hold for arbitrary values of ν and σ_y, respectively, this does not necessarily apply to (3), but for the range of materials used in this study.

ν has a significant influence on the crack formation. The length-to-depth ratio of the crack at load reversal increases with ν (while that of the plastic zone decreases). This has ramifications on the propagation during unloading where only the upper part of the crack opens up so that with decreasing ν the crack loses its characteristic half-penny shape (Figure 12). Analysis results reveal that χ_K decreases approximately linearly with increasing ν (Figure 11).

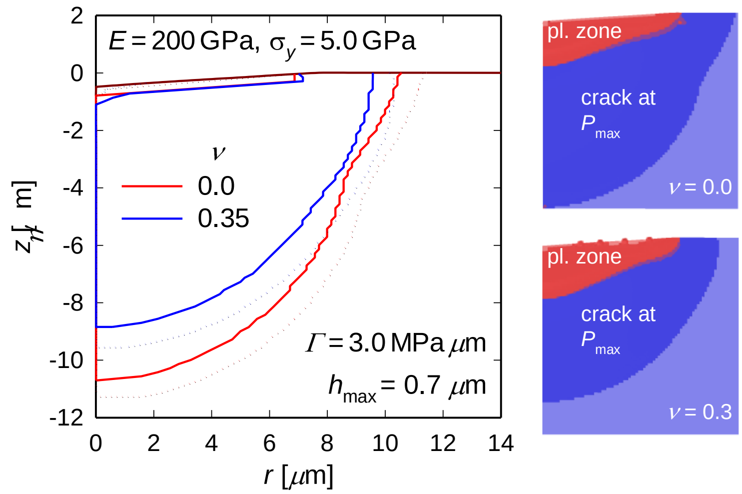

Figure 12. Change of crack shape with Poisson's ratio ν (note that load P_{max} increases with ν for equal depths h_{max}).

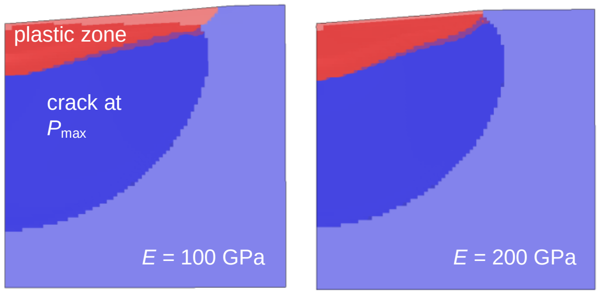

Figure 13. For low *E*, the crack does not grow beyond the plastic zone in radial direction during loading and does not open up during unloading; *E* = 200 GPa for comparison; here the crack will open up during unloading (ν = 0.1, σ_y = 5.0 GPa).

For the lowest E value (100 GPa), the crack does not propagate to the surface during unloading because the crack length in radial direction is smaller than the length of the plastic zone, as shown in Figure 13 for $\nu = 0.1$ and $\sigma_y = 5.0$ GPa. This observation is independent of σ_y, ν, and increasing P_{max} did not change this either. This is in agreement with the study by Petrovic (1983), who reported for glass ceramic (E = 108 GPa) that the length of the crack in radial direction was always slightly below or above a, irrespective of P_{max}. For the highest E (600 GPa), we observe that although damage initiates first in the material, a second (radial) crack initiates at the surface at a later stage of the loading cycle. The radial crack then merges with the median crack. Thus, with increasing E the region of first initiation is expected to move to the surface.

An increase in σ_y is tantamount to an increase in hardness H_K so that the decrease of χ_K with increasing σ_y is in agreement with the proportionality $\chi_K \propto (E/H_K)^{1/2}$.

5. Summary

An XFE model was established that allows the simulation of Knoop indentation cracking. Critical issues associated with cohesive material behavior were discussed and suggestions were made for the viscosity parameter ζ, the damage-initiating threshold $\hat{\sigma}$ and the element size e. The crack evolution was in accordance with experimental findings from the literature. Parameter studies were performed to elucidate the influence of material properties on the crack size and shape. Results serve to predict the fracture toughness of a material from Knoop indentation by taking into account material properties that affect the plastic zone evolution and hence the final crack shape. Knowledge of the final crack shape and size is further essential if the crack is used as a starter crack for crack growth experiments or for the evaluation of in-plane residual stresses.

6. References

1. Abaqus Users' Manual, Version 6.13, Dassault Systèmes Simulia Corp., Providence, RI, 2013.

2. Ahn, Y., Chandrasekar, S. and Farris, T.N., “Determination of Surface Residual Stresses in Machined Ceramics Using Indentation Fracture,” Journal of Manufacturing Science and Engineering, Vol. 118, 1996.
3. Anderson, T.L., “Fracture Mechanics: Fundamentals and Applications,” CRC Press, 2004.
4. Fischer-Cripps, A.C., “Nanoindentation,” Springer New York, 2002.
5. Francois, P., Lefebvre, A. and Vanderschaeve, G., “Low Temperature Plasticity of Brittle Materials: A New Device for Compressive Testing Under Confining Pressure,” Physica Status Solidi (A), Vol. 109, 1988.
6. Gao, Y.F. and Bower, A.F., “A Simple Techniques for Avoiding Convergence Problems in Finite Element Simulations of Crack Nucleation and Growth on Cohesive Interfaces,” Modelling and Simulation in Materials Science and Engineering, Vol. 12, 2004.
7. Hutchinson, J.W. and Evans, A.G., “Mechanics of Materials: Top-down Approaches to Fracture,” *Acta Materialia*, Vol. 48, 2000.
8. Hyun, H.C., Rickhey, F., Lee, J.H., Hahn, J.H. and Lee, H., “Characteristics of Indentation Cracking Using Cohesive Zone Finite Element Techniques for Pyramidal Indenters,” International Journal of Solids and Structures, Vol. 51, 2014.
9. Keer, L.M., Farris, T.N. and Lee, J.-C., “Knoop and Vickers Indentation in Ceramics Analyzed as a Three-Dimentional Fracture,” Journal of the American Ceramic Society, Vol. 69, 1986.
10. Lawn, B.R., Evans, A.G., and Marshall, D.B., “Elastic / Plasic Indentation Damage in Ceramics: the Median / Radial Crack System,” Journal of the American Ceramic Society, Vol. 63, 1980.
11. Lawn, B.R. and Fuller, E.R., “Equilibrium Penny-like Cracks in Indentation Fracture,” Journal of Materials Science, Vol. 10, 1975.
12. Lee, J.H., Gao, Y., Johanns, K.E. and Pharr, G.M., “Cohesive Interface Simulations of Indentation Cracking as a Ftracture Toughness Measurement Method for Brittle Materials,” Acta Materialia, Vol. 60, 2012.
13. Lube, T., “Indentation Crack Profiles in Silicon Nitride,” Journal of the European Ceramic Society, Vol. 21, 2001.
14. Marshall, D.B., Evans, A.G., Khuri Yakub, B.T., Tien, J.W. and Kino, G.S., “The Nature of Machining Damage in Brittle Materials,” Proceedings of the Royal Society of London A, Vol. 385, 1983.
15. Moës, N. and Belytschko, T., “Extended Finite Element Method for Cohesive Crack Growth,” Engineering Fracture Mechanics, Vol. 69, 2002.
16. Mohammadi, S., “Extended Finite Element Method,” Blackwell Publishing, 2008.
17. Petrovic, J.J., “Effect of Indenter Geometry on Controlled-Surface-Flaw Fracture Toughness,” Journal of the American Ceramic Society, Vol. 66, 1983.
18. Ponton, C.B. and Rawlings, R.D., “Vickers Indentation Fracture Toughness Test: Part 1. Review of Literature and Formulation of Standardised Indentation Equations,” Materials Science and Technology, Vol. 5, 1989a.

19. Ponton, C.B. and Rawlings, R.D., “Vickers Indentation Fracture Toughness Test: Part 2. Application and Critical Evaluation of Standardised Indentation Toughness Equations,” Materials Science and Technology, Vol. 5, 1989b.

20. Quin, G.D. and Bradt, R.C., “On the Vickers Indentation Fracture Toughness Test,” Journal of the American Ceramic Society, Vol. 90, 2007.

21. Rice, J.R., “A Path Independent Integral and the Approximate Analysis of Strain Concentration by Notches and Cracks,” Journal of Applied Mechanics, Vol. 35, 1968.

22. Tomar, V., Zhai, J. and Zhou, M., “Bounds for Element Size in a Variable Stiffness Cohesive Finite Element Model,” International Journal for Numerical Methods in Engineering, Vol. 61, 2004.

Appendix

c^* can be estimated based on the following notions: (1) E_{dmg} is invariant of $\hat{\sigma}$; (2) the damage and crack shapes are independent of $\hat{\sigma}$. The sum of damages D over all elements n multiplied by the corresponding element area, here e^2, is

$$\sum_n e^2 D_n \approx \frac{E_{dmg}}{\Gamma} \tag{6}$$

Invoking assumption (1), this must be equal to the ideally brittle case. Thus,

$$\sum_n e^2 D_n = k\, c^{*\,2} \tag{7}$$

where k is a parameter describing the shape of the damage/crack area. Since k is independent of $\hat{\sigma}$ (assumption 2), k can be obtained from the finite $\hat{\sigma}$ case, *i.e.*

$$k\left(c + L_{DZ}\right)^2 = \sum_i e^2 H\left(D_i\right) \quad ; \quad H\left(D_i\right) = \begin{cases} 1 & \text{for } D_i > 0 \\ 0 & \text{for } D_i = 0 \end{cases} \tag{8}$$

where L_{DZ} is given in Equation (4). Solving for k and inserting the resulting expression into Equation (7), we get

$$c^* = \left(c + L_{DZ}\right)\sqrt{\sum_n e^2 D_n \Big/ \sum_i e^2 H\left(D_i\right)} \tag{9}$$

Using the value of output StatusXFEM for D we get for our reference material $c^* \approx 11.81\ \mu$m ($h_{\max}$ = 0.8 μm).

Acknowledgement

This work was supported by the Basic Science Research Program through the National Research Foundation of Korea (No. NRF-2012 R1A2A2A 01046480).